PHOTONICS Research

Adaptive optics wavefront correction using a damped transpose matrix of the influence function

Boyu Gu[1,2,3] and Yuhua Zhang[1,2,*]

[1]Doheny Eye Institute, Pasadena, California 91103, USA
[2]Department of Ophthalmology, University of California - Los Angeles, Los Angeles, California 90095, USA
[3]Currently at School of Computer and Information Engineering, Tianjin Chengjian University, Tianjin 300384, China
*Corresponding author: yzhang@doheny.org

Received 29 December 2021; revised 23 April 2022; accepted 24 April 2022; posted 25 April 2022 (Doc. ID 452364); published 30 June 2022

To assess the performance of adaptive optics and predict an optimal wavefront correction, we built a wavefront reconstructor with a damped transpose matrix of the influence function. Using an integral control strategy, we tested this reconstructor with four deformable mirrors in an experimental system, an adaptive optics scanning laser ophthalmoscope, and an adaptive optics near-confocal ophthalmoscope. Testing results proved that this reconstructor could ensure a stable and precise correction for wavefront aberration compared to a conventional optimal reconstructor formed by the inverse matrix of the influence function. This method may provide a helpful tool for testing, evaluating, and optimizing adaptive optics systems.

https://doi.org/10.1364/PRJ.452364

1. INTRODUCTION

Adaptive optics (AO) was initially conceived to restore the spatial resolution of large astronomical telescopes by compensating for time-varying wave aberrations of the imaging light in the atmosphere [1]. In the 1990s, it was adopted to improve the resolution of retinal imaging [2]. Now AO has been employed by a variety of ophthalmic imagining modalities, including flood illumination fundus cameras [2], scanning laser ophthalmoscopy [3], and optical coherence tomography [4,5]. The function of AO in ophthalmoscopy is to correct for wavefront aberrations of the imaging light caused by the eye's optical defects, thereby enabling retinal imaging to achieve diffraction-limited (or near-diffraction-limited) resolution through a dilated pupil [6].

A classical AO system may consist of a wavefront corrector that "nulls" wavefront aberration of the imaging light and a wavefront sensor (WS) that measures the aberration. A typical wavefront corrector is a deformable mirror (DM), and a conventional WS is a Shack–Hartmann sensor [7–9]. Although new methods such as wavefront sensorless AO [10–13] and computational AO [14] have evolved in the past decade, an AO system comprising a DM and a Shack–Hartmann WS remains a major practical regime for most applications in clinical ophthalmoscopy and vision science research [6]. This configuration is especially suitable for correcting wavefront aberration in the human eye's optical system, which can vary with a temporal frequency greater than 30 Hz [15–21].

During AO operation, the surface of the DM is controlled to generate a shape that can minimize the wavefront aberration [9]. The DM surface is shaped by a summation of the actuations from all actuators. This process can be described by a system equation: $\boldsymbol{W} = \boldsymbol{A}\boldsymbol{X}$, where $\boldsymbol{A}$ is a matrix describing the contribution of individual actuators to the wavefront, namely, the influence function matrix (IFM). $\boldsymbol{X}$ is a vector of the driving commands (voltage or current) to the actuators, and $\boldsymbol{W}$ is a vector of the wavefront aberrations measured by the WS [7–9]. The IFM can be obtained by recoding the DM's response to the actuation of an individual actuator [22]. Once the IFM is determined, the driving commands to the DM actuators can be derived from the system equation and executed through a specific control strategy [9]; for example, the integral control algorithm has been the most used method in ophthalmic AO systems [6,7]. Regardless of the differences among various control strategies, the inverse of IFM is an essential component for building the wavefront reconstructor, i.e., to derive the driving command vector for the DM actuators from measured wave aberration [9].

Since the wavefront sampling points outnumber the DM actuators in a practical AO system, $\boldsymbol{A}\boldsymbol{X} = \boldsymbol{W}$ is overdetermined and does not have a unique solution. Therefore, the commands to the actuators calculated from the wavefront aberration should be a solution to the system equation that can best fit the wavefront shape. In a general form, the command vector can be $\boldsymbol{X} = \boldsymbol{A}^{+}\boldsymbol{W}$, where $\boldsymbol{A}^{+}$ is the pseudoinverse (Moore–Penrose inverse) of $\boldsymbol{A}$ and can be favorably obtained by singular

value decomposition (SVD) [23]. However, the IFM of a practical AO system may be ill-conditioned due to spatial mismatch between actuators of the DM and sampling points of the WS, wavefront measurement error, and the inter-actuator coupling. Thus, errors and noise in the wavefront measurement can be amplified significantly by small singular values and result in divergence of the wavefront reconstruction [24,25]. Therefore, proper regularization must be applied to suppress the impact of small singular values [9,26]. Methods such as waffle or Kolmogorov model penalty [22] and damped least-squares control [27,28] have been reported to build the wavefront reconstructors of ophthalmic AO.

Truncated SVD (TSVD) has mathematically and experimentally proved to be a favorable method for computing the pseudoinverse of a matrix that is ill-conditioned or close to being singular among many regularization methods [29–32]. In this method, small singular values are set to zero, i.e., truncated, to minimize noise perturbation. However, it is difficult to determine an optimal condition number for discarding the small singular values since singular values can be influenced by the overall configuration of an AO imaging system and the measurement error and noise of the WS. Therefore, an optimal TSVD is often determined heuristically through trials with different condition numbers.

In this study, we present a practical approach for assessing and predicting the best achievable wavefront correction of an AO system, thereby providing a reference for building an optimal TSVD wavefront reconstructor. We evaluated the method with four DMs of three constitutional types in an AO testing system, an AO scanning laser ophthalmoscope (AOSLO), and an AO near-confocal ophthalmoscope (AONCO).

2. METHOD

A. Wavefront Reconstruction

1. Wavefront Reconstructor Using a Damped Transpose Matrix of the IFM

Assuming that an AO system consists of a Shack–Hartmann WS and a DM, the WS measures the wavefront over M sub-apertures. The DM nulls the wavefront aberration with N actuators. The IFM $\boldsymbol{A}$ is a real matrix with a dimension of $M \times N$. By SVD, $\boldsymbol{A}$ can be factorized in the form

$$\boldsymbol{A} = \boldsymbol{U}\boldsymbol{\Sigma}\boldsymbol{V}^{\mathrm{T}}, \tag{1}$$

where $\boldsymbol{U}$ is an $M \times M$ real matrix, and $\boldsymbol{V}$ is an $N \times N$ real matrix. The columns of $\boldsymbol{U}$ and $\boldsymbol{V}$ are left and right singular vectors for $\boldsymbol{A}$, respectively. Both $\boldsymbol{U}$ and $\boldsymbol{V}$ are orthonormal matrices, i.e., $\boldsymbol{U}\boldsymbol{U}^{\mathrm{T}} = \boldsymbol{I}_M$, $\boldsymbol{V}\boldsymbol{V}^{\mathrm{T}} = \boldsymbol{I}_N$, $\boldsymbol{U}^{\mathrm{T}}$ and $\boldsymbol{V}^{\mathrm{T}}$ are transposes of $\boldsymbol{U}$ and $\boldsymbol{V}$, respectively; $\boldsymbol{I}_M$ and $\boldsymbol{I}_N$ are $M \times M$ and $N \times N$ identity matrices, respectively. $\boldsymbol{\Sigma}$ is a diagonal matrix with elements consisting of singular values (σ_i) in the economy size form with non-zero rows only:

$$\boldsymbol{\Sigma} = \begin{bmatrix} \sigma_1 & 0 & \cdots & 0 \\ 0 & \sigma_2 & \cdots & 0 \\ \vdots & \vdots & & \vdots \\ 0 & 0 & \cdots & \sigma_r \end{bmatrix}, \tag{2}$$

where σ_r is determined by the rank of the IFM and the machine precision in numerical computation. Given a wavefront aberration vector $\boldsymbol{W}$, the command vector of DM actuators can be obtained by

$$\boldsymbol{X} = \boldsymbol{A}^{+}\boldsymbol{W} = (\boldsymbol{U}\boldsymbol{\Sigma}\boldsymbol{V}^{\mathrm{T}})^{+}\boldsymbol{W} = \boldsymbol{V}\boldsymbol{\Sigma}^{+}\boldsymbol{U}^{\mathrm{T}}\boldsymbol{W}, \tag{3}$$

$$\boldsymbol{\Sigma}^{+} = \begin{bmatrix} 1/\sigma_1 & 0 & \cdots & 0 \\ 0 & 1/\sigma_2 & \cdots & 0 \\ \vdots & \vdots & & \vdots \\ 0 & 0 & \cdots & 1/\sigma_r \end{bmatrix}, \tag{4}$$

$$\boldsymbol{X} = \boldsymbol{V}\begin{bmatrix} 1/\sigma_1 & 0 & \cdots & 0 \\ 0 & 1/\sigma_2 & \cdots & 0 \\ \vdots & \vdots & & \vdots \\ 0 & 0 & \cdots & 1/\sigma_r \end{bmatrix}\boldsymbol{U}^{\mathrm{T}}\boldsymbol{W}. \tag{5}$$

Equation (5) shows the process in which a vector $\boldsymbol{W} \in \mathbb{R}^M$ transforms to $\boldsymbol{X} \in \mathbb{R}^N$, where $\mathbb{R}^M$ and $\mathbb{R}^N$ indicate M- and N-dimensional space, respectively. During the transformation, matrices $\boldsymbol{U}$ and $\boldsymbol{V}$ rotate the vector $\boldsymbol{W}$, and the matrix $\boldsymbol{\Sigma}^{+}$ scales the vector $\boldsymbol{W}$, from space $\mathbb{R}^M$ to $\mathbb{R}^N$. The transformation is susceptible to small singular values (σ_i), which amplifies measurement errors, causing unstable AO control or an inaccurate correction for wavefront aberration. TSVD sets a certain number of small singular values in $\boldsymbol{\Sigma}$ to zero to avoid this. However, the determination is system dependent and may be arbitrary.

Here, we propose to use a damped transpose matrix of the IFM $\boldsymbol{A}$ to build the wavefront reconstructor:

$$\boldsymbol{X} = c\boldsymbol{A}^{\mathrm{T}}\boldsymbol{W}, \tag{6}$$

where c is a DM-dependent damping factor, and $\boldsymbol{A}^{\mathrm{T}}$ is the transpose matrix of the IFM:

$$\boldsymbol{A}^{\mathrm{T}} = (\boldsymbol{U}\boldsymbol{\Sigma}\boldsymbol{V}^{\mathrm{T}})^{\mathrm{T}} = \boldsymbol{V}(\boldsymbol{\Sigma}^{\mathrm{T}})\boldsymbol{U}^{\mathrm{T}}, \tag{7}$$

$$X = V\begin{bmatrix} c\sigma_1 & 0 & \cdots & 0 \\ 0 & c\sigma_2 & \cdots & 0 \\ \vdots & \vdots & & \vdots \\ 0 & 0 & \cdots & c\sigma_r \end{bmatrix}U^{\mathrm{T}}W. \tag{8}$$

In this process, we keep the singular value matrices $\boldsymbol{U}$ and $\boldsymbol{V}$ but damp the singular values, i.e., the vector $\boldsymbol{W} \in \mathbb{R}^M$ is transformed into the space $\mathbb{R}^N$ with the exact rotation directions as determined by singular matrices $\boldsymbol{U}$ and $\boldsymbol{V}$, but the lengths of the bases are scaled with damped singular values ($c\sigma_i$). Using an integral control algorithm, actuator commands can be calculated from light spot deflections (i.e., wavefront slopes) [16] on each sub-aperture, in the form

$$\boldsymbol{X}_i = c\boldsymbol{A}^{\mathrm{T}}\boldsymbol{W} + \boldsymbol{X}_{i-1}, \tag{9}$$

where i indicates the control loops; it is a zonal correction since the driving commands of the actuators are calculated from the deflections of the light spots on each sub-aperture of the pupil plane [16]. Therefore, this method will be referred to as "Zonal[TM]" (zonal correction using the transpose matrix of the influence function) throughout the paper.

When the wavefront is expressed using the Zernike polynomials ($\boldsymbol{W} = \sum_{j=1}^{m} a_j \boldsymbol{Z}_j$) (or modes) [33], wavefront aberrations are corrected modally. The command signal is in the form

$$\boldsymbol{X}_i = c\left[\boldsymbol{A}^{\mathrm{T}} \sum_{j=1}^{m} a_j \begin{bmatrix} \partial \boldsymbol{Z}_j/\partial x \\ \partial \boldsymbol{Z}_j/\partial y \end{bmatrix}\right] + \boldsymbol{X}_{i-1}, \tag{10}$$

where a_j is the coefficient of the jth Zernike mode, and $\boldsymbol{Z}_j$ is a vector of the jth Zernike polynomial. This method will be referred to as "Modal[TM]" (modal correction using the transpose matrix of the influence function) in the paper.

2. Wavefront Reconstructor Using the Inverse of IFM with TSVD

We also tested AO performance using a reconstructor built with an inverse of the IFM with optimal TSVD and operated with the same integral control strategy. In the zonal correction,

$$\boldsymbol{X}_i = g\boldsymbol{A}^{+}\boldsymbol{W} + \boldsymbol{X}_{i-1}, \tag{11}$$

where i indicates the control loops, g is the gain factor of the integrator, and $0 < g < 1$. This method will be referred to as "Zonal[IM]" (zonal correction using the inverse matrix of the influence function) throughout the paper.

In the modal control mode, the command signal is

$$\boldsymbol{X}_i = g\left[\boldsymbol{A}^{+} \sum_{j=1}^{m} a_j \begin{bmatrix} \partial \boldsymbol{Z}_j/\partial x \\ \partial \boldsymbol{Z}_j/\partial y \end{bmatrix}\right] + \boldsymbol{X}_{i-1}, \tag{12}$$

where a_j and $\boldsymbol{Z}_j$ have the same meaning as those in Eq. (10); this method will be referred to as "Modal[IM]" (modal correction using the inverse matrix of the influence function).

B. Evaluation of the Performance of AO Using Different Wavefront Reconstructors

To verify the methods, we tested four DMs, including two magnetic DMs with 97 actuators (Hi-Speed DM97, ALPAO SAS, Montbonnot-Saint-Martin, France), one electromagnetic DM with 52 actuators (Mirao 52e, Imagine-Optic, Co., Orsay, France), and one piezo DM with 40 actuators (DMP40/M-P01, Thorlabs Inc., Newton, New Jersey), as shown in Fig. 1. One of the ALPAO DMs is a part of the AO system in the high-speed AONCO reported by Lu *et al.* [34]. This DM and Thorlabs DMP 40 were evaluated in the AO testbed described next. The testing data are presented in Figs. 2–7. The second ALPAO DM97 and DM Mirao 52e are parts of the AOSLO developed at the University of Alabama at Birmingham (UAB AOSLO) by Yu *et al.* [20]. Therefore, these two DMs were evaluated in this instrument. The testing results are presented in Figs. 8 and 9. Finally, we also assessed ALPAO DM97 in the AONCO. The results are shown in Fig. 10.

1. AO Testing System

As shown in Fig. 1, the light emitted from a diode laser (QFBGLD-730-20S, QPhotonics, Ann Arbor, MI) is collimated (by L1) and sets a pupil diameter of 5.4 mm (by an iris diaphragm S). The collimated light passes through a beam splitter (BS) and reaches the DM through a telescope (L2 and L3) that expands the beam diameter to match the DM. For the Thorlabs DMP40 DM, the magnification ratio of the telescope is two. For ALPAO DM97, the magnification ratio is 2.5. The

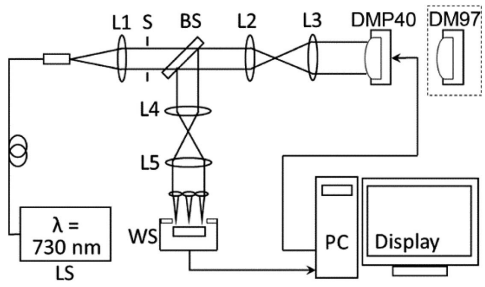

Fig. 1. Adaptive optics testing system. LS, laser source; L1–L5, lenses; S, optical aperture; BS, beam splitter; WS, wavefront sensor.

light is then reflected by the DM along the ingoing path back to the BS, which reflects 50% of the light to a custom-made Shack–Hartmann WS through a telescope (L4 and L5) that expands the beam diameter to 7.2 mm. The WS consists of a lenslet array (0300-7.6-S, Adaptive Optics Associates, Cambridge, MA) and a complementary metal–oxide semiconductor (CMOS) camera (MV1-D1312-160-CL-12, PhotonFocus AG, Switzerland). The lenslet has a square aperture of 300 μm × 300 μm and a focal length of 7.6 mm. The pixel size of the CMOS camera is 8 μm × 8 μm. Over the pupil, the WS measures the wavefront through 448 sub-apertures (sampling points).

2. AOSLO

The UAB AOSLO has been reported in detail elsewhere [20]. The working principle and technical characteristics are summarized here for the readers' convenience.

The UAB AOSLO operates with a confocal scanning imaging regime. The imaging light source is a low coherence superluminescent diode (SLD) (Broadlighter S840-HP, Superlum Ltd., Ireland) with a central wavelength of 840 nm and spectral bandwidth of 50 nm. Light emitted from the SLD is first collimated and then fed into the scanning optics (which include the AO components) to the eye, generating a 2D scanning raster on the retina. Light scattered back from the retina following the ingoing path transmits into the image acquisition module. The imaging light is focused through a pinhole onto a photomultiplier tube (PMT) that converts the imaging light to an electric signal. Finally, a computer acquires the video signal and generates real-time retina images. The AO system consists of two DMs: one is the Mirao 52e, and the other is an ALPAO DM97-15 (not the same one in the AO testing system). The two DMs in the AOSLO can be operated independently. The AO system has a custom Shack–Hartmann WS similar to the one used in the testing system described above. The WS measures the wave aberration by 193 sampling points over a pupil of 6.0 mm (diameter). The DM compensates for the wave aberration at a closed-loop frequency of 110 Hz with custom control algorithms. In most eyes, the root mean square (RMS) of the wave aberration after AO compensation can be as low as 0.04 μm, less than 1/14 of the light wavelength for wavefront sensing. Therefore, the imaging can be considered diffraction limited. The AOSLO has an imaging field of view inside the human eye of 1.5° × 1.5°. The image is

digitized by 512 × 512 pixels. Retinal images can be acquired at a 15 or 30 frames/second frame rate.

3. AONCO

The AONCO [34–36] employs an SLD (Broadlighter S795-HP, Superlum Ltd., Russia) with a central wavelength of 795 nm and spectral bandwidth of 15 nm. Light emitted from the SLD is first collimated and then focused by a cylindrical lens to form a light line on a digital micromirror device (Texas Instruments, DLP 0.55 XGA Series 450 DMD, Dallas, USA), which modulates the line illumination intensity to create a line of point sources. The modulated beam is fed into the scanning optics and projects a 2D scanning pattern on the retina. Backscattered light from the retina following the ingoing path transmits to a high-speed line camera (spL2048-140km, Basler Co., Germany). The AO consists of an ALPAO DM97 (the one tested in the AO testbed in this study) and a custom Shack–Hartmann WS that measures the wavefront aberration by 193 sampling points over a pupil of 6.75 mm (diameter). The AONCO's imaging field of view inside the human eye is 1.2° × 1.2°. The image is digitized by 512 × 512 pixels. Retinal images can be acquired at a 200 frames/second frame rate.

4. Metrics for Evaluation of the Performance of AO

The AO performance was assessed by two metrics. The first one is the RMS of wavefront aberrations, calculated from the root sum square of the coefficients of the Zernike modes:

$$\mathrm{RMS}_{\mathrm{Zernike}} = \sqrt{\sum_{j=1}^{m} a_j^2}. \tag{13}$$

The second parameter is the RMS of deflections of light spots on all sub-apertures of the Shack–Hartmann WS:

$$\mathrm{RMS}_{\mathrm{deflection}} = \sqrt{\sum_{i=1}^{n} (\Delta x_i^2 + \Delta y_i^2)/n}, \tag{14}$$

where n is the number of sub-apertures, and Δx_i and Δy_i are light spot deflections in the horizontal and the vertical directions, respectively, within the ith sub-aperture.

In all systems, we measured the $\mathrm{RMS}_{\mathrm{Zernike}}$ and $\mathrm{RMS}_{\mathrm{deflection}}$. In the AOSLO, we also evaluated the brightness of the retinal image of a model eye. The model eye consists of a spherical lens with a focal length of 100 mm and a piece of diffuse white paper placed on the focal plane mimicking the retina. The image brightness was defined as the mean value of all pixels. The images were acquired with a 1.5° × 1.5° field of view over which the model retina was illuminated uniformly by the imaging light. In all experiments using different wavefront reconstructors, the settings of the photodetector (such as gain) and image digitizer (such as bits and blank level) remained the same. Thus, the image brightness measures the light power on the photodetector, which depends on the wave aberration correction. Better AO correction enabled more light to reach the photodetector, thereby higher image brightness.

We evaluated the AO performance using different wavefront reconstructors with a series of ophthalmic trial lenses of various spherical and cylindrical powers (−0.5 D to −2.25 D). These trial lenses were placed in the model eye's pupil plane and mimicked the human eye's wave aberration. The image brightness was recorded before and after AO compensation for wave aberration.

In the AONCO, we evaluated the brightness of the retinal image using the same model eye. The images were acquired with a field of view of 1.2° × 1.2°. The camera's gain and blank level remained the same in all experiments.

5. Influence Function Measurement

The IFM was measured by recording the light spot deflections generated by pushing and pulling each actuator of the DM sequentially in all sub-apertures of the WS. To the actuation of the ith actuator, the wavefront recorded by the WS, i.e., the influence function, was

$$\boldsymbol{A}_i = \left(\begin{bmatrix} B_i^{x\ \mathrm{push}} \\ B_i^{y\ \mathrm{push}} \end{bmatrix} - \begin{bmatrix} B_i^{x\ \mathrm{pull}} \\ B_i^{x\ \mathrm{pull}} \end{bmatrix} \right) / 2p, \tag{15}$$

where $\boldsymbol{B}_i^x$ and $\boldsymbol{B}_i^y$ are light spot deflections in horizontal and vertical directions, respectively, superscripts "push" and "pull" indicate the moving direction of the actuator, and p is the value of the command applied to the actuator.

Assuming the DM has N actuators, the IFM $\boldsymbol{A}$ was organized as

$$\boldsymbol{A} = [\boldsymbol{A}_1, \boldsymbol{A}_2, \cdots, \boldsymbol{A}_N]. \tag{16}$$

3. RESULTS

A. Influence Function Matrices of Different Deformable Mirrors

The IFM of the AO testing system with Thorlabs DMP40 exhibits a sinusoidal pattern [Fig. 2(a)]. The correlation matrix of the IFM discloses the interaction between actuators [Fig. 2(b)]. Matrix elements with large values were along the main diagonal. Two bright lines beside the main diagonal indicate that an actuator strongly influences its neighboring wavefront (DM surface). The number of the preserved (optimal) SVD values is 28 [Fig. 2(c)], which was determined by a series of trials with different condition numbers. The data distribution of the transpose matrix of the IFM [Fig. 2(d)] shows a high similarity to that of the inverse matrix of the IFM with an optimal TSVD [Fig. 2(e)].

For the IFM of ALPAO DM97, elements with large values appeared mainly in the central diagonal region [Fig. 3(a)]. The correlation matrix of the IFM [Fig. 3(b)] reveals the impact of an actuator on its neighboring wavefront. The data distribution pattern of the IFM transpose of ALPAO DM97 [Fig. 3(d)] is also highly similar to that of the inverse of IFM with an optimal TSVD [Fig. 3(e)].

We assessed the similarity between the transpose and the inverse matrices of the IFM with the optimal TSVD using the normalized cross-correlation coefficient:

$$r(\boldsymbol{P}, \boldsymbol{Q}) = \frac{\sum_{i,j} (p_{i,j} - p_m)(q_{i,j} - q_m)}{\sqrt{\sum_{i,j} (p_{i,j} - p_m)^2 \sum_{i,j} (q_{i,j} - q_m)^2}}, \tag{17}$$

where r is the correlation coefficient of two matrices $\boldsymbol{P}$ and $\boldsymbol{Q}$, $p_{i,j}$ and $q_{i,j}$ are the elements in the jth column of the ith row in $\boldsymbol{P}$ and $\boldsymbol{Q}$, respectively, and p_m and q_m are the means of $\boldsymbol{P}$ and $\boldsymbol{Q}$, respectively. We also compared the similarity between the

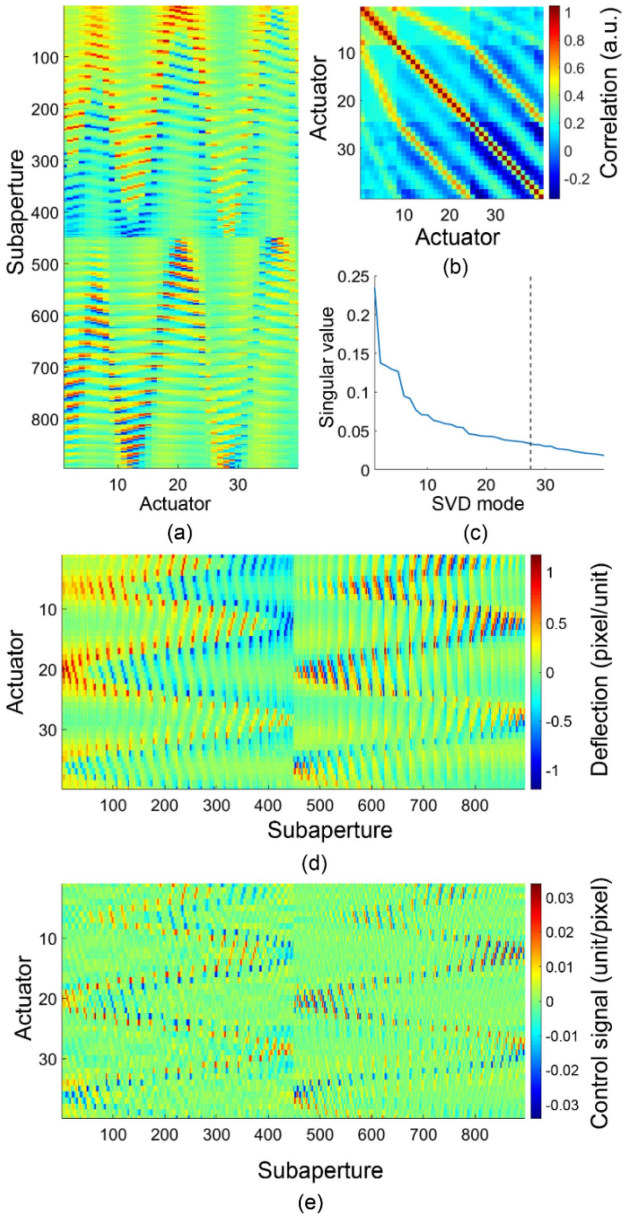

Fig. 2. Influence function of the adaptive optics testing system with deformable mirror Thorlabs DMP40. (a) Influence function matrix (IFM). (b) Correlation matrix of IFM. (c) Singular values of the IFM, the dashed line indicates the optimal number of truncated singular values (modes). (d) Transpose matrix of IFM. (e) The inverse of the IFM with truncated singular value decomposition (TSVD) at the singular value indicated in (c). The color bar in (d) also applies to (a).

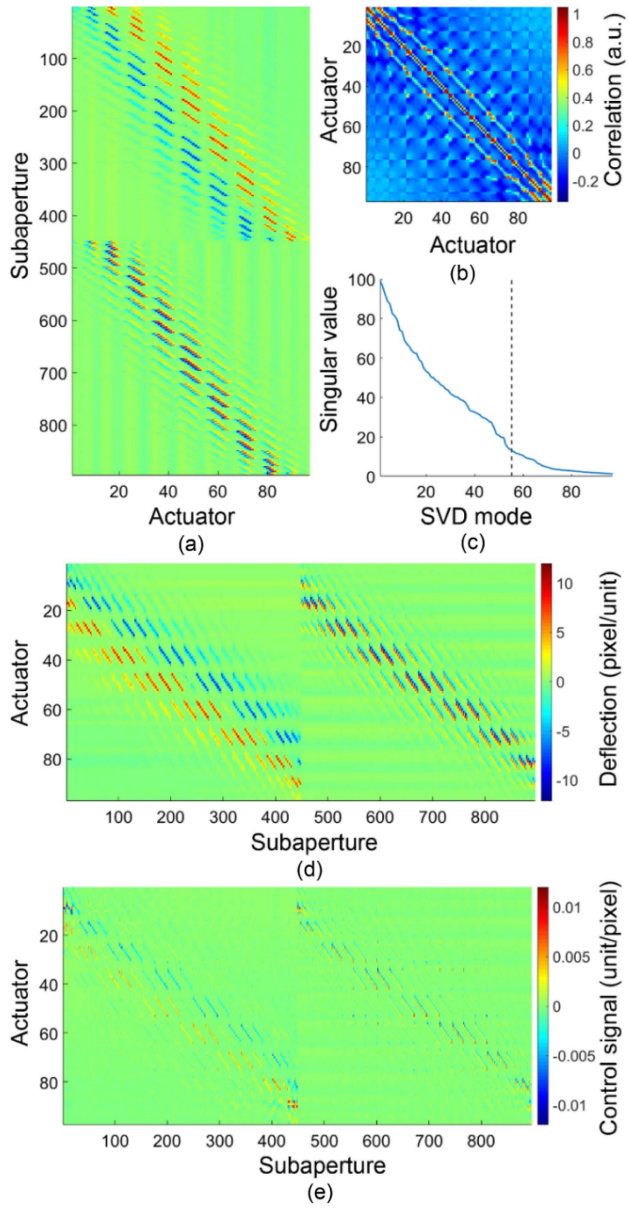

Fig. 3. Influence function of the adaptive optics testing system with deformable mirror ALPAO DM97. (a) Influence function matrix (IFM). (b) Correlation matrix of IFM. (c) Singular values of the IFM, the dashed line indicates the optimal number of truncated singular values (modes). (d) Transpose matrix of IFM. (e) The inverse of the IFM with truncated singular value decomposition (TSVD) at the singular value indicated in (c). The color bar in (d) also applies to (a).

inverse matrix of the IFM with the optimal TSVD and with all singular values (untruncated).

The correlation coefficients between the transpose IFM and the inverse IFM with the optimal TSVD are 0.62 and 0.53 for Thorlabs DMP40 and ALPAO DM97, respectively. On the other hand, the coefficients of correlation between the inverse IFM with the optimal TSVD and with the total singular values are only 0.42 and 0.11 for Thorlabs DMP40 and ALPAO DM97, respectively.

B. AO Performance in the Testing System

Using a wavefront reconstructor built with an inverse matrix of IFM truncated at different SVD modes, the AO system performed differently (Fig. 4). When more singular values (from maximum to minimum) were preserved, the AO control system could not maintain a stable control loop or could not correct the wavefront aberration accurately. For ALPAO DM97, if 10 or 18 minor SVD modes were truncated, the AO correction became divergent [Fig. 4(a), red and black dotted lines].

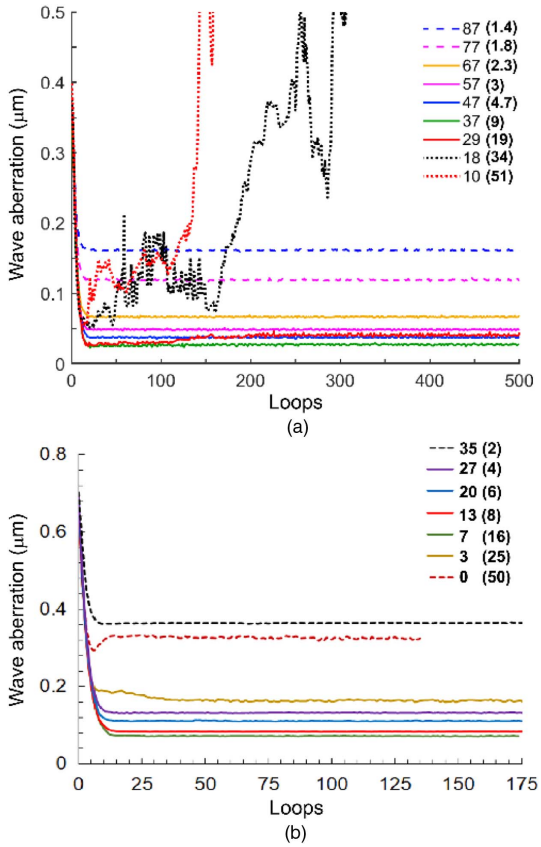

Fig. 4. Adaptive optics (AO) correction for wavefront aberration using wavefront reconstructors built with truncated single value decomposition (TSVD) of the influence function matrix. The AO was operated to flatten the deformable mirrors from their free (unpowered) state in the AO testing system shown in Fig. 1. The AO worked with a closed-loop integral controller. (a) Data were recorded using the ALPAO DM97 deformable mirror. (b) Data were acquired using the Thorlabs DMP40 deformable mirror. The numbers outside the parentheses indicate how many singular values were set to zero (i.e., truncated). Those in the parentheses are corresponding condition numbers (ratio of maximum singular value over minimum singular value).

The AO achieved an optimal performance by trimming 37 small singular values, yielding the smallest residual wavefront aberration [Fig. 4(a), solid green line]. With more singular values truncated, while the AO could maintain a stable closed loop, the residual wavefront aberration increased [Fig. 4(a), solid orange lines, magenta, and blue dashed lines]. For Thorlabs DMP40, while keeping all singular values did not result in a divergent AO, the AO could not achieve an optimal compensation for the wavefront aberration [Fig. 4(b), red dashed line]. The AO performed the optimal correction when 7 or 13 small singular values were set to zeros [Fig. 4(b), solid green and red lines]. The residual wavefront aberration increased when more singular values were set to zero.

When AO operated with the reconstructors using the inverse of IFM with TSVD, the integrator's gain factor was set to 0.3 for both DMs.

The AO using the damped transpose IFM reconstructor yielded smaller residual wavefront aberration than AO using the optimal TSVD reconstructor (Fig. 5). However, it took more time for the former to reach the minimal wave aberration (typically ~100 loops) than for the latter (~10 loops). The results were consistent for both Thorlabs DMP40 and ALPAO DM97 and zonal and modal control modes.

The damping factor is determined by the mechanical and electrical properties of the DM. It was heuristically derived from the influence of an actuator on the wavefront area where the nearest neighboring actuator has maximum impact. For ALPAO DM97, the peak influence function, measured by the deflection of the light centroids on the WS, was 11.98 pixels/unit, where "unit" is the control command unit of the actuator with no dimension. The influence of this actuator on the wavefront area where its nearest neighboring actuator locates (1.5 mm away) is 6.47 pixels/unit. The response threshold of the DM is 5×10^{-4} units. Therefore, to avoid influencing its neighboring area, the actuation stroke of an actuator should be damped by $5 \times 10^{-4}/6.47 = 7.73 \times 10^{-4}$ times. We found that within the range of 10^{-5} to 10^{-4}, the AO worked well with the reconstructor using the damped transpose IFM. The damping factor for Thorlabs DM40 was estimated in the same way and within the range of $1 \times 10^{-2} - 5 \times 10^{-2}$.

In our experiments, we selected $c = 2.4 \times 10^{-5}$ for ALPAO DM97 and $c = 4.8 \times 10^{-2}$ for Thorlabs DMP40 by trial and error.

The gain factor (0.3) for the reconstructor using the inverse of IFM with TSVD was an optimal value obtained from our previous studies [20,34–37], chosen by a trade-off among (high) stability, (short) converging time, and (minimal) residual

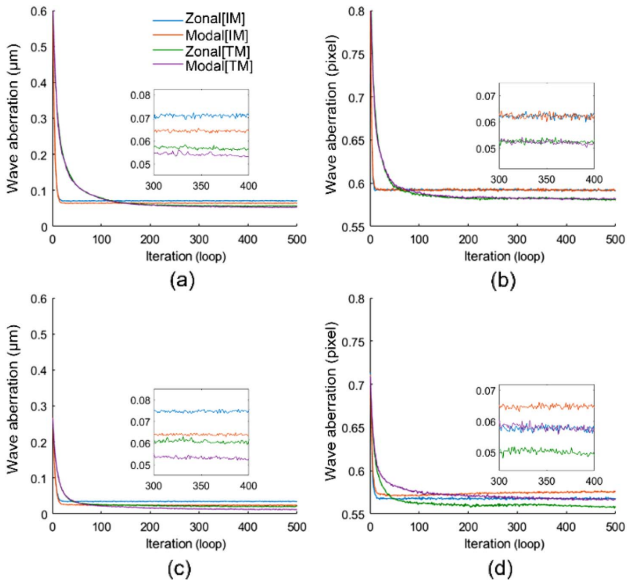

Fig. 5. Adaptive optics (AO) correction for wave aberration using different reconstructors and deformable mirrors. The AO was performed to flatten the deformable mirror from its free (unpowered) state. (a), (b) Testing results of AO using the Thorlabs DMP40. The wavefront aberration was measured in μm (a) and in the root mean square (RMS) of the pixel numbers of the centroids of deflections (b). (c), (d) Data of AO using the ALPAO DM97. The wavefront aberration was measured in μm (c) and the RMS of the centroids of deflections in pixel numbers (d). Color legends in (a) apply to all panels.

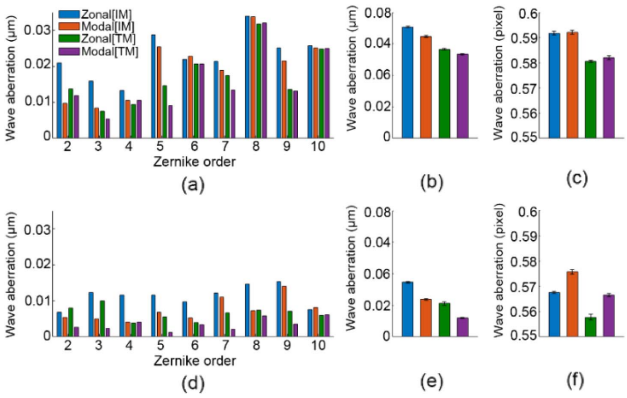

Fig. 6. Residual wave aberration after adaptive optics correction using different reconstructors and deformable mirrors. AO was performed to flatten the deformable mirror from its free (unpowered) state. (a)–(c) Results obtained from the Thorlabs DMP40. (a) Root mean square (RMS) of coefficients of the 2nd to 10th orders of Zernike modes. (b) RMS of all Zernike coefficients. (c) Residual wavefront aberration was assessed by the RMS of the centroids of deflections in all sub-apertures of the wavefront sensor, measured in pixel numbers. (d)–(f) Results from the ALPAO DM97. (d) RMS of coefficients of the 2nd to 10th orders of Zernike modes. (e) RMS of all Zernike coefficients. (f) Residual wave aberration was assessed by RMS of centroids of deflections measured in pixel numbers. The residual aberrations in (b), (c), (e), and (f) were averaged from the last five (496th–500th) loops of AO correction. Error bars indicate standard deviations. Color legends in (a) apply to all panels.

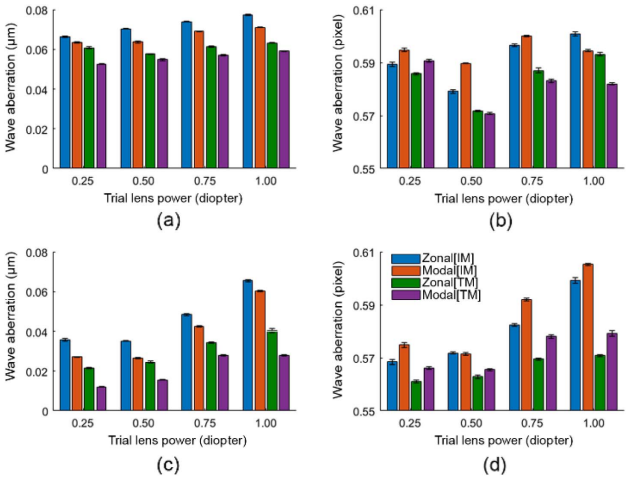

Fig. 7. Evaluation of the performance of adaptive optics (AO) using different reconstructors. The AO system was tested under various wavefront aberrations introduced by placing spherical trial lenses at a plane conjugate to the deformable mirror. (a), (b) Results for the AO using the Thorlabs DMP40. (a) RMS of the residual aberration measured by all Zernike modes in μm. (b) RMS of the centroid deflections in all sub-apertures of the wavefront sensor, measured in pixel numbers. (c), (d) Results for AO using the DM ALPAO DM97. (c) RMS of the residual aberration measured by all Zernike modes in μm. (d) RMS of the light centroid deflections measured in pixel numbers. The residual aberrations were averaged from the last five (496th–500th) loops of AO correction. Error bars indicate standard deviations. Color legends in (d) apply to all panels.

wave aberration. The damping factor was selected by considering the same determinants. Experiments have shown that residual wave aberrations exhibited no significant difference after AO correction when the gain or the damping factor varies within the same magnitude.

Figure 6 shows that the AO using the transpose IFM reconstructor yielded smaller residual aberration than AO using the optimal TSVD inverse IFM reconstructor in most of the Zernike modes for both ALPAO DM97 and Thorlabs DMP40. ALPAO DM97 made a better correction [Figs. 6(d)–6(f)] than Thorlabs DMP40 [Figs. 6(a)–6(c)], especially in compensating for higher-order aberrations [Figs. 6(a) and 6(d)].

AO correction using the Zonal[TM] method had superior performance to that using an optimal TSVD reconstructor under different levels of initial wave aberration (Fig. 7). In

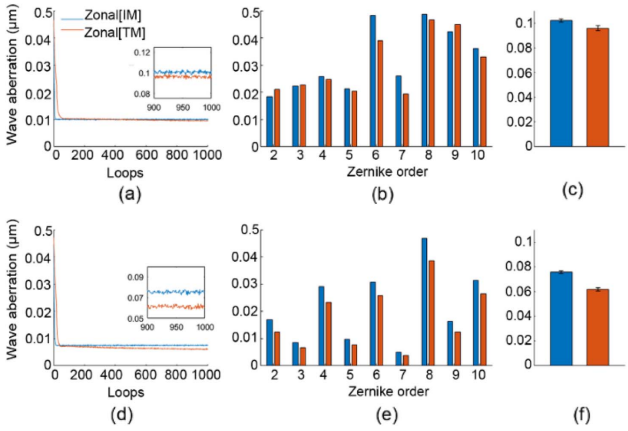

Fig. 8. Adaptive optics using different reconstructors tested in the adaptive optics scanning laser ophthalmoscope (AOSLO). The AO was performed to correct the system wavefront aberration of the AOSLO when the deformable mirrors were unpowered. (a)–(c) Results tested with the deformable mirror Mirao 52e. (d)–(f) Data of deformable mirror ALPAO DM97. The residual aberrations in (c) and (f) were averaged from the last five (996th–1000th) loops of AO correction. Error bars indicate standard deviations. Color legends in (a) apply to all panels.

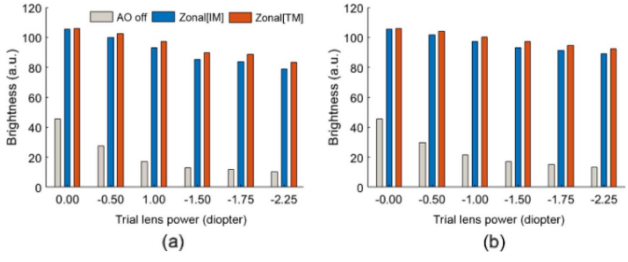

Fig. 9. Evaluation of adaptive optics (AO) performance using different reconstructors in the adaptive optics scanning laser ophthalmoscope (AOSLO). The brightness of the model eye's retinal image was measured before and after AO correction for wavefront aberration. The wavefront aberration was introduced by placing a trial lens at the pupil plane of the model eye. (a), (b) Image brightness improvement by AO compensation for spherical and cylindrical wave aberrations. Color legends in (a) apply to all panels. This test was done with the ALPAO DM97 deformable mirror.

addition, the ALPAO DM97 demonstrated a better performance than the Thorlabs DMP40.

C. AO Performance in the UAB AOSLO

We used a damping factor of 2.4×10^{-5} for both ALPAO DM97 and Mirao 52e. As shown in Fig. 8, AO using the Zonal[TM] reconstructor yielded smaller residual aberration in most Zernike modes for both DMs. The results are consistent with that obtained in the AO testing system. ALPAO DM97 demonstrated a better correction than Mirao 52e.

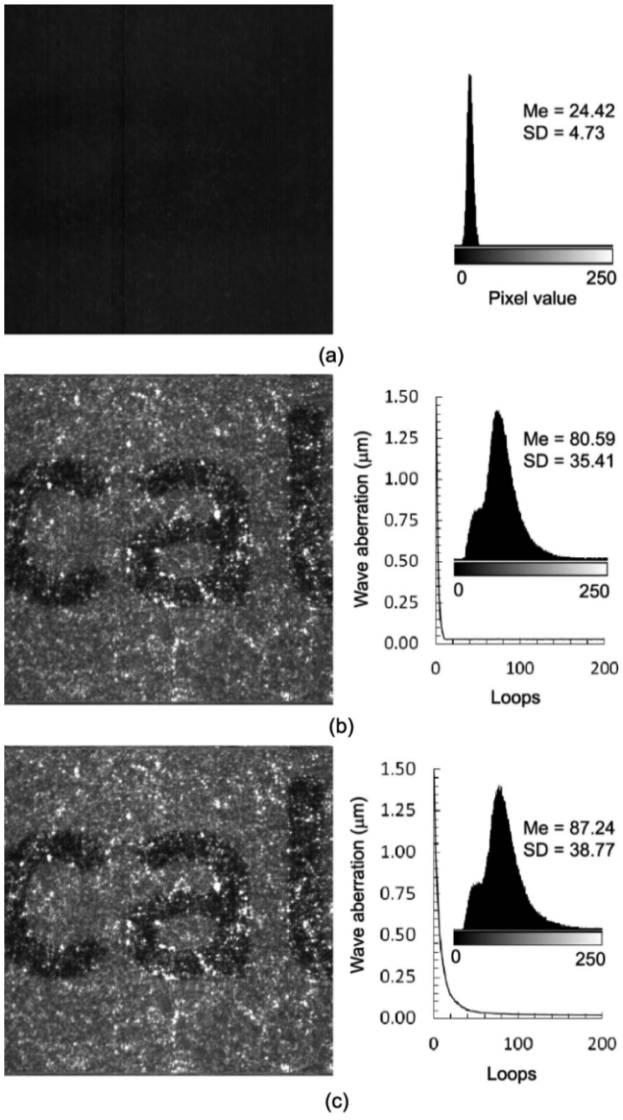

Fig. 10. Evaluation of adaptive optics (AO) performance using different reconstructors in the adaptive optics near-confocal ophthalmoscope (AONCO). Retinal images of the model eye were acquired before and after AO correction for wavefront aberration. The wavefront aberration was introduced by placing a spherical trial lens at the pupil plane of the model eye. (a) Retinal image of the model eye and its histogram before AO correction. (b) Using the Zonal[IM] wavefront reconstructor and a gain factor of 0.3, the model eye retinal image and its histogram after AO correction. (c) AO correction using the Zonal[TM]. The root mean square (RMS) initial wavefront aberration was 1.50 μm.

As shown in Fig. 9, the Zonal[TM] reconstructor in the AOSLO produced brighter retinal images than the Zonal[IM] reconstructor by 2.61%–5.84% in correction for wavefront aberration introduced by spherical lenses and by 2.46%–4.18% in correction for wavefront aberration introduced by cylindrical lenses. AO using ALPAO DM97 had better correction than AO using Mirao 52e.

D. AO Performance in the AONCO

We used a damping factor of 2.4×10^{-5} for ALPAO DM97. As shown in Fig. 10, AO correction for wavefront aberration increased the brightness and enhanced the model eye retinal image resolution. For example, with an initial wavefront aberration of 1.50 μm, the Zonal[TM] reconstructor made a better residual aberration (0.16 μm versus 0.20 μm) and higher brightness (mean 87.24 versus 80.59) than the Zonal[IM].

4. DISCUSSION

We have developed a method for AO wavefront reconstruction using a damped transpose IFM. We validated the methods with four DMs of three different types in different AO settings and with varying wavefront aberrations.

We can appreciate the mathematical basis underlying the wavefront reconstructor using a damped transpose IFM from the process that seeks the DM actuator command to null a measured wavefront, described by Eq. (3). The IFM $\boldsymbol{A}$ is a space transformer that converts the DM command vector $\boldsymbol{X} \in \mathbb{R}^N$ to the wavefront vector $\boldsymbol{W} \in \mathbb{R}^M$ by rotating (governed by the unitary singular value matrices $\boldsymbol{U}$ and $\boldsymbol{V}^T$) and scaling (controlled by the diagonal matrix $\boldsymbol{\Sigma}$ consisting of the singular values) the vector. Compared to the general solution of the AO system equation using SVD [Eq. (5)], the reconstructor using a damped transpose IFM employed the same singular value matrices $\boldsymbol{U}$ and $\boldsymbol{V}$ of the IFM but damped the singular values [Eq. (8)]. In other words, the vector $\boldsymbol{W} \in \mathbb{R}^M$ was transformed into space $\mathbb{R}^N$ with the same rotation as SVD, but its length was scaled with damped singular values. Thus, this reconstructor is essentially a regulated inverse of the IFM, which can be seen from the high similarity between the transpose IFM and the inverse IFM with the optimal TSVD [Figs. 2(d) and 2(e), Figs. 3(d) and 3(e)]. However, we must acknowledge that this analysis is intuitive, and the IFM is dependent on a specific DM configuration. Therefore, a rigorous mathematical analysis is warranted in future studies.

AO compensation for wavefront aberration using a reconstructor with a damped transpose IFM can be perceived as an iterative process. The wavefront is flattened by adjusting individual actuators to minimize the local wavefront aberrations guided by wavefront measurement. In each loop, while an actuator attempts to reduce the wavefront aberration at the actuator's location, it also affects its neighboring wavefront. This influence can be mitigated by applying a damping factor. Through several loops, the wave aberration is reduced to the level limited by the noise of the WS. Since the diagonal matrix is suboptimal compared to the one in TSVD, AO operating with this reconstructor requires more loops to minimize the wavefront aberration than AO using a reconstructor based on an optimal inverse IFM.

The damped transpose IFM based reconstructor has proved two advantages. First, it is intrinsically tolerant to noise perturbation compared to a classical reconstructor using an inverse of the IFM since it does not involve an inverse of the singular values of the IFM [Eq. (8)]. Thus, noise and errors in wavefront measurement will not be amplified by minor singular modes and are suppressed by the damping factor. Therefore, this reconstructor ensures a stable AO closed loop, leading to a steady reduction of the wavefront aberration. By contrast, in a reconstructor using the inverse IFM, small singular values may amplify noise and errors in wavefront measurement [Eq. (5)] and result in divergence of the control loop. Second, the reconstructor using the damped transpose IFM can better correct wavefront aberration than the reconstructor using the inverse IFM with an optimal TSVD, as demonstrated in all experiments in the AO testing system, the AOSLO, and the AONCO. This advantage may be because the damped transpose IFM reconstructor does not discard any singular values and uses contributions from all actuators of the DM.

Rigorous mathematical analysis and simulation have proved that TSVD is a favorable method with a robust ability to cope with noise perturbation in ill-conditioned systems [29–31]. In previous research, we testified that the wavefront reconstructor using the inverse IFM with an optimal TSVD has an excellent performance equal to the reconstructors using the inverse IFM with advanced regularization methods [22,38] in various AO retinal imaging instruments [20,34–37,39]. Our experimental investigation in this study has proved that the reconstructor using a damped transpose IFM has a superior performance to that using an optimal TSVD inverse of the IFM. Thus, the method presented in this study can be used to predict the best achievable wavefront correction for an AO system.

The limitation of the new reconstructor is apparent. It takes longer for the AO system to minimize wavefront aberration than the classical reconstructor using an optimal TSVD inverse IFM. For example, as shown in Fig. 5, AO with the TSVD reconstructor could minimize the wave aberration in ~10 loops, whereas AO using the damped transpose IFM took ~30–100 loops. Thus, this reconstructor may not be suitable for correcting rapid time-varying wavefront aberrations. However, in applications dealing with static or slow-varying wave aberrations, such as AO microscopy [40], our method may provide a practical and robust correction for wavefront aberrations. The reconstructor using the damped transpose IFM cannot replace the classical wavefront reconstructor but offers a helpful tool for AO system testing, especially at the initial stage of developing an AO imaging system.

5. CONCLUSION

We present a wavefront correction method using a damped transpose of the IFM. This method may be used for AO system testing, evaluation, and optimization. In addition, it may be potentially employed in applications that use AO to compensate for static or slow-varying aberrations.

Funding. Research to Prevent Blindness/Dr. H. James and Carole Free Catalyst Award for Innovative Research Approaches for AMD; National Eye Institute (R01EY024378); W. M. Keck Foundation; Carl Marshall and Mildred Almen Reeves Foundation.

Disclosures. The authors declare no conflicts of interest.

Data Availability. Data underlying the results presented in this paper may be obtained from the authors upon reasonable request.

REFERENCES

1. H. W. Babcock, "The possibility of compensating astronomical seeing," Publ. Astron. Soc. Pac. **65**, 229–236 (1953).
2. J. Liang, D. R. Williams, and D. T. Miller, "Supernormal vision and high-resolution retinal imaging through adaptive optics," J. Opt. Soc. Am. A **14**, 2884–2892 (1997).
3. A. Roorda, F. Romero-Borja, W. Donnelly Iii, H. Queener, T. Hebert, and M. Campbell, "Adaptive optics scanning laser ophthalmoscopy," Opt. Express **10**, 405–412 (2002).
4. R. J. Zawadzki, S. M. Jones, S. S. Olivier, M. Zhao, B. A. Bower, J. A. Izatt, S. Choi, S. Laut, and J. S. Werner, "Adaptive-optics optical coherence tomography for high-resolution and high-speed 3D retinal in vivo imaging," Opt. Express **13**, 8532–8546 (2005).
5. Y. Zhang, J. Rha, R. Jonnal, and D. Miller, "Adaptive optics parallel spectral domain optical coherence tomography for imaging the living retina," Opt. Express **13**, 4792–4811 (2005).
6. S. Marcos, J. S. Werner, S. A. Burns, W. H. Merigan, P. Artal, D. A. Atchison, K. M. Hampson, R. Legras, L. Lundstrom, G. Yoon, J. Carroll, S. S. Choi, N. Doble, A. M. Dubis, A. Dubra, A. Elsner, R. Jonnal, D. T. Miller, M. Paques, H. E. Smithson, L. K. Young, Y. Zhang, M. Campbell, J. Hunter, A. Metha, G. Palczewska, J. Schallek, and L. C. Sincich, "Vision science and adaptive optics, the state of the field," Vision Res. **132**, 3–33 (2017).
7. J. Porter, H. Queener, J. Lin, K. Thorn, and A. A. S. Awwal, *Adaptive Optics for Vision Science: Principles, Practices, Design, and Applications* (Wiley-Interscience, 2006).
8. F. Roddier, *Adaptive Optics in Astronomy* (Cambridge University, 1999).
9. R. K. Tyson, *Principles of Adaptive Optics*, 4th ed. (CRC Press/Tylor and Francis Group, 2010).
10. M. J. Booth, "Wavefront sensorless adaptive optics for large aberrations," Opt. Lett. **32**, 5–7 (2007).
11. H. Hofer, N. Sredar, H. Queener, C. Li, and J. Porter, "Wavefront sensorless adaptive optics ophthalmoscopy in the human eye," Opt. Express **19**, 14160–14171 (2011).
12. Y. Jian, J. Xu, M. A. Gradowski, S. Bonora, R. J. Zawadzki, and M. V. Sarunic, "Wavefront sensorless adaptive optics optical coherence tomography for *in vivo* retinal imaging in mice," Biomed. Opt. Express **5**, 547–559 (2014).
13. K. F. Tehrani, J. Xu, Y. Zhang, P. Shen, and P. Kner, "Adaptive optics stochastic optical reconstruction microscopy (AO-STORM) using a genetic algorithm," Opt. Express **23**, 13677–13692 (2015).
14. S. G. Adie, B. W. Graf, A. Ahmad, P. S. Carney, and S. A. Boppart, "Computational adaptive optics for broadband optical interferometric tomography of biological tissue," Proc. Natl. Acad. Sci. USA **109**, 7175–7180 (2012).
15. H. Hofer, P. Artal, B. Singer, J. L. Aragon, and D. R. Williams, "Dynamics of the eye's wave aberration," J. Opt. Soc. Am. A **18**, 497–506 (2001).
16. H. Hofer, L. Chen, G. Y. Yoon, B. Singer, Y. Yamauchi, and D. R. Williams, "Improvement in retinal image quality with dynamic correction of the eye's aberrations," Opt. Express **8**, 631–643 (2001).
17. T. Nirmaier, G. Pudasaini, and J. Bille, "Very fast wave-front measurements at the human eye with a custom CMOS-based Hartmann-Shack sensor," Opt. Express **11**, 2704–2716 (2003).
18. L. Diaz-Santana, C. Torti, I. Munro, P. Gasson, and C. Dainty, "Benefit of higher closed-loop bandwidths in ocular adaptive optics," Opt. Express **11**, 2597–2605 (2003).

19. A. Mira-Agudelo, L. Lundstrom, and P. Artal, "Temporal dynamics of ocular aberrations: monocular vs binocular vision," Ophthalmic Physiol. Opt. **29**, 256–263 (2009).
20. Y. Yu, T. Zhang, A. Meadway, X. Wang, and Y. Zhang, "High-speed adaptive optics for imaging of the living human eye," Opt. Express **23**, 23035–23052 (2015).
21. E. Gofas-Salas, P. Mece, C. Petit, J. Jarosz, L. M. Mugnier, A. Montmerle Bonnefois, K. Grieve, J. Sahel, M. Paques, and S. Meimon, "High loop rate adaptive optics flood illumination ophthalmoscope with structured illumination capability," Appl. Opt. **57**, 5635–5642 (2018).
22. K. Y. Li, S. Mishra, P. Tiruveedhula, and A. Roorda, "Comparison of control algorithms for a MEMS-based adaptive optics scanning laser ophthalmoscope," in *Proceedings American Control Conference* (2009), pp. 3848–3853.
23. A. Ben-Israel and T. N. E. Greville, *Generalized Inverses: Theory and Applications*, CMS Books in Mathematics (Springer Verlag, 2003), p. 420.
24. D. L. Fried, "Least-square fitting a wave-front distortion estimate to an array of phase-difference measurements," J. Opt. Soc. Am. **67**, 370–375 (1977).
25. R. H. Hudgin, "Wave-front reconstruction for compensated imaging," J. Opt. Soc. Am. **67**, 375–378 (1977).
26. J. W. Hardy, *Adaptive Optics for Astronomical Telescopes* (Oxford University, 1998).
27. W. Zou, X. Qi, and S. A. Burns, "Woofer-tweeter adaptive optics scanning laser ophthalmoscopic imaging based on Lagrange-multiplier damped least-squares algorithm," Biomed. Opt. Express **2**, 1986–2004 (2011).
28. W. Zou, X. Qi, G. Huang, and S. A. Burns, "Improving wavefront boundary condition for *in vivo* high resolution adaptive optics ophthalmic imaging," Biomed. Opt. Express **2**, 3309–3320 (2011).
29. P. C. Hansen, "The truncated SVD as a method for regularization," BIT Numer. Math. **27**, 534–553 (1987).
30. P. C. Hansen, "Solution of Ill-Posed Problems by Means of Truncated SVD," in *Numerical Mathematics Singapore 1988*, R. P. Agarwal, Y. M. Chow, and S. J. Wilson, eds. (Birkhäuser Basel, 1988), pp. 179–192.
31. I. F. Gorodnitsky and B. D. Rao, "Analysis of error produced by truncated SVD and Tikhonov regularization methods," in *Proceedings of 28th Asilomar Conference on Signals, Systems and Computers* (1994), Vol. **21**, pp. 25–29.
32. E. Fernandez and P. Artal, "Membrane deformable mirror for adaptive optics: performance limits in visual optics," Opt. Express **11**, 1056–1069 (2003).
33. Y. Zhang, S. Poonja, and A. Roorda, "MEMS-based adaptive optics scanning laser ophthalmoscopy," Opt. Lett. **31**, 1268–1270 (2006).
34. J. Lu, B. Gu, X. Wang, and Y. Zhang, "High speed adaptive optics ophthalmoscopy with an anamorphic point spread function," Opt. Express **26**, 14356–14374 (2018).
35. J. Lu, B. Gu, X. Wang, and Y. Zhang, "Adaptive optics parallel near-confocal scanning ophthalmoscopy," Opt. Lett. **41**, 3852–3855 (2016).
36. J. Lu, B. Gu, X. Wang, and Y. Zhang, "High-speed adaptive optics line scan confocal retinal imaging for human eye," PLoS ONE **12**, e0169358 (2017).
37. A. Meadway, C. A. Girkin, and Y. Zhang, "A dual-modal retinal imaging system with adaptive optics," Opt. Express **21**, 29792–29807 (2013).
38. W. Zou and S. A. Burns, "Testing of Lagrange multiplier damped least-squares control algorithm for woofer-tweeter adaptive optics," Appl. Opt. **51**, 1198–1208 (2012).
39. Y. Yu and Y. Zhang, "Dual-thread parallel control strategy for ophthalmic adaptive optics," Chin. Opt. Lett. **12**, 121202 (2014).
40. M. J. Booth, "Adaptive optical microscopy: the ongoing quest for a perfect image," Light Sci. Appl. **3**, e165 (2014).